



Identifying Three New AGNs among Fermi Unidentified Giga-electronvolt Sources

Shun-Hao Ji¹, Zhong-Xiang Wang^{1,2}, Qiang-Meng Huang¹, and Ruo-Heng Yang¹

¹ Department of Astronomy, School of Physics and Astronomy, Yunnan University, Kunming 650091, China; jishunhao@mail.ynu.edu.cn, wangzx20@ynu.edu.cn

² Shanghai Astronomical Observatory, Chinese Academy of Sciences, Shanghai 200030, China
Received 2024 April 21; revised 2024 June 12; accepted 2024 June 20; published 2024 July 11

Abstract

We report our identification of three giga-electronvolt γ -ray sources, 4FGL J0502.6+0036, 4FGL J1055.9+6507, and 4FGL J1708.2+5519, as Active Galactic Nuclei (AGNs). They are listed in the latest Fermi-Large Area Telescope source catalog as unidentified ones. We find that the sources all showed γ -ray flux variations in recent years. Using different survey catalogs, we are able to find a radio source within the error circle of each source's position. Further analysis of optical sources in the fields allows us to determine the optical counterparts, which showed similar variation patterns to those seen in γ -rays. The optical counterparts have reported redshifts of 0.6, 1.5, and 2.3, respectively, estimated from photometric measurements. In addition, we also obtain an X-ray spectrum of 4FGL J0502.6+0036 and a flux upper limit on the X-ray emission of 4FGL J1055.9+6507 by analyzing the archival data. The broadband spectral energy distributions of the three sources from radio to γ -rays are constructed. Comparing mainly the γ -ray properties of the three sources with those of different sub-classes of AGNs, we tentatively identify them as blazars. Followup optical spectroscopy is highly warranted for obtaining their spectral features and thus verifying the identification.

Key words: gamma-rays: galaxies – (galaxies:) BL Lacertae objects: general – (galaxies:) quasars: general

1. Introduction

Active Galactic Nuclei (AGNs) are powered by accretion onto supermassive black holes (SMBHs) in the centers of galaxies. Approximately 10% of AGNs have radio jets, and the jet formation is widely considered due to two mechanisms: the Blandford–Znajek mechanism (Blandford & Znajek 1977), in which the jet extracts the rotational energy of an SMBH, and the Blandford–Payne mechanism (Blandford & Payne 1982), in which the jet extracts the rotational energy of an accretion disk surrounding the SMBH. Depending on our viewing angle of AGNs with jets, or so-called radio-loud AGNs, they can be divided into two classes (e.g., Urry & Padovani 1995). The first are blazars when our viewing angles of their jets are small (generally $\leq 10^\circ$). Blazars are further divided into two sub-types, BL Lac objects (BL Lacs) and Flat Spectrum Radio Quasars (FSRQs). BL Lacs have very weak or no emission lines in their optical emission, while FSRQs show emission lines with equivalent widths greater than 5 \AA (Urry & Padovani 1995; Scarpa & Falomo 1997). Due to the small viewing angles and thus strong Doppler boosting effect, blazars are bright and highly variable sources in the sky. The second class of radio-loud AGNs are misaligned ones (MAGNs), for which we have large viewing angles. They tend to be fainter and usually closer to us than blazars. MAGNs are further classified into radio galaxies (RGs) and Steep Spectrum Radio Quasars.

The Large Area Telescope (LAT) onboard *the* Fermi Gamma-ray Space Telescope (Fermi) has been monitoring the high-energy γ -ray sky since 2008 (Atwood et al. 2009). There are 7194 γ -ray sources in energy range of from 50 MeV to 1000 GeV listed in the updated fourth source catalog (4FGL-DR4; Ballet et al. 2023). Nearly 66% of them can be associated with a known astrophysical object, and among the associated ones, more than 80% are either blazars or MAGNs, with 55 being the latter. These AGN sources offer a good sample for various studies, for example, the contributions of blazars and MAGNs to the extragalactic γ -ray background (e.g., Di Mauro et al. 2014, 2018; Ajello et al. 2015; Ackermann et al. 2016; Fukazawa et al. 2022), the blazar sequence (e.g., Ghisellini & Tavecchio 2008; Fan et al. 2017; Ghisellini et al. 2017), and strong variabilities (e.g., Ghisellini et al. 2013; Hayashida et al. 2015; Patel et al. 2018; Shukla et al. 2018). For the other 34% of unidentified sources, blazars should dominate them and there may be a small number of MAGNs, according to the proportions of the associated sources. Identification of these sources can help build the γ -ray sample as completely as possible, thus helping probe the full physical properties of AGNs. A popular way for source identification is through statistical analysis or machine-learning methods (e.g., Yi et al. 2017; Chiaro et al. 2021; Kaur et al. 2023; Zhu et al. 2024), and by focusing on variations of optical light curves (R. Yang et al. 2024, in preparation), we have tested when developing our machine-learning method. In

addition, we are also carrying out identification of the most likely AGN sources found in machine-learning through multi-wavelength analysis. The companion work serves to cross check the results of the machine-learning method. Also, identification of individual sources could reveal hidden cases that deserve full studies because of interesting physical properties and processes.

In this paper, we report the identification of three new AGNs among 4FGL-DR4 sources through our multi-wavelength analysis. They are 4FGL J0502.6+0036, 4FGL J1055.9+6507, and 4FGL J1708.2+5519. This paper is organized as follows. Section 2 describes the multi-wavelength data we used in the analysis. Section 3 describes the analysis we conducted and provides the results. We discuss the likely nature of the three sources in Section 4.

2. Multi-wavelength Data

2.1. Optical and Mid-infrared Data

Optical imaging and optical light-curve data were obtained from the Panoramic Survey Telescope and Rapid Response System (Pan-STARRS; Chambers et al. 2016) and the Zwicky Transient Facility (ZTF; Bellm et al. 2019) respectively. To obtain good-quality light curves, we selected magnitude data points by requiring $catflags = 0$ and $\chi < 4$; the magnitudes are in the ZTF g - and r -band (zg and zr respectively). In addition, the mid-infrared (MIR) light-curve data were obtained from the NEOWISE Single-exposure Source Database (Mainzer et al. 2014), where the bands are WISE w1 ($3.4 \mu\text{m}$) and w2 ($4.6 \mu\text{m}$).

The ZTF magnitudes are in the AB photometric system (Bellm et al. 2019), very similar to those provided in Pan-STARRS (Medford et al. 2020). The MIR magnitudes are in the Vega system, and their conversion to fluxes can be calculated by using the given zero-magnitude flux density (Wright et al. 2010).

2.2. X-Ray Data

For the fields of the three Fermi γ -ray sources, we searched for archival X-ray data. There were a few observations of the fields of 4FGL J0502.6+0036 and 4FGL J1055.9+6507 conducted with the X-Ray Telescope (XRT) onboard the Neil Gehrels Swift Observatory (Swift). The observation information is summarized in Table 1.

Using the online Swift-XRT data products generator tool³ (for details about the online tool, see Evans et al. 2007, 2009, 2020), we ran source detection in the XRT data. All the data for each of the two source fields were combined, and only the counterpart to 4FGL J0502.6+0036 (see below Section 3.1) was weakly detected. Its 0.3–10 keV spectrum was extracted. We fitted the spectrum with an absorbed power-law (PL) model in XSPEC 12.12.1 using the C-Statistic method,

³ https://www.swift.ac.uk/user_objects/

Table 1
Information for the Swift-XRT Observations

Date	Obsid	Exposure (s)	$F_{0.3-10}^{\text{unabs}}/10^{-13}$ ($\text{erg cm}^{-2} \text{s}^{-1}$)
4FGL J0502.6+0036			
2019-04-20	3107436001	1236	
2024-02-15	3112553001	4323	
2024-02-17	3112553003	5110	
2024-02-19	3112553005	1799	$1.4^{+1.3}_{-0.6}$
2024-02-21	3112553007	576	
2024-02-22	3112553009	287	
2024-02-25	3112553011	1012	
2024-02-27	3112553013	174	
4FGL J1055.9+6507			
2024-03-06	3112558001	69	
2024-03-15	3112558003	455	$\leq 10.6^a$
2024-04-04	3112558013	232	

Note.

^a Indicates the 3σ flux upper limit.

where the Galactic hydrogen column density N_{H} was fixed at $8.57 \times 10^{20} \text{cm}^{-2}$ (HI4PI Collaboration et al. 2016).

For 4FGL J1055.9+6507, no counterpart was found (see below Section 3.2). Using the longest exposure (455 s; Table 1), we obtained a 3σ upper limit on the count rate at the source position. To convert it to an upper limit on the 0.3–10 keV flux, we used the PIMMS tool⁴ by assuming a PL spectrum with a photon index of 2, where $N_{\text{H}} = 2.25 \times 10^{20} \text{cm}^{-2}$ (HI4PI Collaboration et al. 2016) toward the source direction was used.

2.3. Fermi-LAT Data and Source Model

The Fermi-LAT data used were 0.1–500 GeV photon events (evclass = 128 and evtype = 3) from the updated Fermi Pass 8 database in a time range from 2008 August 4 15:43:36 (UTC) to 2023 November 1 09:31:26.8104 (UTC). The region of interest (RoI) for each target was set to be $20^\circ \times 20^\circ$ centered at the position given in 4FGL-DR4. To avoid the contamination from the Earth limb, we excluded the events with zenith angles $> 90^\circ$. We set the expression $DATA_QUAL > 0 \&\& LAT_CONFIG == 1$ to select good time-interval events. In our analysis, the package FermiTools2.2.0 and the instrument response function P8R3_SOURCE_V3 were used.

The source models for the targets were generated based on 4FGL-DR4. The three targets were all modeled as a point source with a PL spectrum, $dN/dE = N_0(E/E_0)^{-\Gamma}$, where E_0 values were fixed at 1.74 GeV, 1.35 GeV, and 1.4 GeV, respectively, for 4FGL J0502.6+0036, 4FGL J1055.9+6507, and 4FGL J1708.2+5519. We adopted the same spectral models in our source models for them. In addition, all sources

⁴ <https://cxc.harvard.edu/toolkit/pimms.jsp>

in 4FGL-DR4 within 25° of a target were included. We set the spectral indices and normalizations of the sources within 5° of a target as free parameters and fixed the other parameters at the catalog values. We also included the extragalactic diffuse emission and the Galactic diffuse emission components, for which the spectral files `iso_P8R3_SOURCE_V3_v1.txt` and `gll_iem_v07.fits` were used respectively. The normalizations of the two components were always set as free parameters in our analysis.

3. Analysis and Results

3.1. 4FGL J0502.6+0036

Using the source model described above, we performed the standard binned likelihood analysis on the data in 0.1–500 GeV for 4FGL J0502.6+0036. The obtained best-fit $\Gamma = 2.13 \pm 0.14$, with a test statistic (TS) value of $\simeq 54$. The Γ value is consistent with that given in 4FGL-DR4, but the TS value is lower than 83 in 4FGL-DR4. The discrepancy in TS values is likely caused by our inclusion of the latest data, during which the source was not detectable (see Figures 1 and A1). With the best-fit model, we extracted the source’s light curve with 90 day time bins. In the extraction by performing the maximum likelihood analysis on the data of each time bin, only the normalization parameters of the sources within 5° of the target were set free and the other parameters were fixed at the best-fit values obtained in the analysis of the whole data. The whole light curve is depicted in Figure A1. As can be seen, there was a flare during the approximate time period of MJD 58600–59750 (see Figure 1). We also calculated the variability index TS_{var} (Nolan et al. 2012) of the light curve, and obtained $TS_{\text{var}} \approx 179.3$. The index value indicates variability of the source at a 7.4σ significance level (as TS_{var} is considered to be distributed as χ^2 , with 61 degrees of freedom).

To connect 4FGL J0502.6+0036 with its multi-wavelength counterparts, we ran `gtfindsrc` in Fermitools to determine the source’s position. We obtained R.A. = $75^\circ 65'$, decl. = $+0^\circ 61'$ (equinox J2000.0), with a 2σ uncertainty of $0^\circ 06'$. This position is consistent with that given in 4FGL-DR4 (see Table 2). Within the error circle of the position, we found only one radio source, BWE 0500+0034, in the SIMBAD database. We employed the tool `gtsrcid` in Fermitools (Abdo et al. 2010) to estimate the probability of 4FGL J0502.6+0036 in association with BWE 0500+0034. The calculated probability was 97.8%, suggesting a highly likely association between them, given that Fermi-LAT used a threshold of 80% to determine associations for point sources. The 0.1–500 GeV TS map of the source field, centered at 4FGL J0502.6+0036, during the flare time period (MJD 58600–59750) was calculated. The TS map, displayed in the left panel of Figure 2, helps indicate the positional coincidence between 4FGL J0502.6+0036 and BWE 0500+0034. The latter has a 95%-confidence radius of $\sim 50''$ (Becker et al. 1991).

Using the Pan-STARRS $100'' \times 100''$ image centered at BWE 0500+0034 (right panel of Figure 2), we examined optical sources in the field for the potential counterpart. There are more than ten sources, and we obtained their ZTF and WISE MIR light curves to check their flux variations. The optical source closest to the center of BWE 0500+0034, called PS1 in this work (Figure 2), exhibited concurrent brightening activity during the flaring time period of 4FGL J0502.6+0036 (Figure 1). Because of the temporal and spatial coincidence, BWE 0500+0034 and PS1 are thus the likely radio and optical counterparts respectively.

3.2. 4FGL J1055.9+6507

By performing the standard binned likelihood analysis on the data in 0.1–500 GeV for 4FGL J1055.9+6507, we obtained the best-fit parameters, in which $\Gamma = 2.25 \pm 0.08$, with a TS value of $\simeq 168$. The values are in agreement with those given in 4FGL-DR4. Using the same setting as those for 4FGL J0502.6+0036, we extracted its 90 day binned light curve (see Figure A1). The light curve also shows flare-like events, which mostly occurred during MJD 58500–60250 in recent years (Figure 1). The variability index TS_{var} was found to be ≈ 260.2 , which indicates source variability at a 10.6σ significance level. Thus, the source was also significantly variable.

Running `gtfindsrc` to check the source’s position, we obtained R.A. = $163^\circ 92'$, decl. = $+65^\circ 14'$ (equinox J2000.0), with a 2σ uncertainty of $0^\circ 04'$ (see Table 2). Further checking radio sources as the possible candidate counterpart, there is only one found, given in the NRAO VLA Sky Survey (NVSS) catalog (Condon et al. 1998) as NVSS J105533+650956. Running `gtsrcid`, we obtained an association probability of 98.8% between 4FGL J1055.9+6507 and NVSS J105533+650956, also indicating their association is highly likely. We also calculated the TS map in 0.1–500 GeV during the flaring time period for the source field (left panel of Figure 3). The TS map illustrates the positional matches between 4FGL J1055.9+6507 and the radio source. The Pan-STARRS $10'' \times 10''$ image (Figure 3), in *i*-band centered at NVSS J105533+650956, was obtained to search for the possible optical counterpart. There is one source, named PS2, in the error region of NVSS J105533+650956. We note that PS2, with its position given in Pan-STARRS as the average of multiple exposures in multiple bands, is 0.3 off the peak of the optical source in the *i*-band image (Figure 3). This offset could reflect the systematic positional uncertainty in astrometry of Pan-STARRS (a nearly the same offset was found in the next case 4FGL J1708.2+5519; see Section 3.3). The optical source’s ZTF and WISE light curves were obtained and are shown in Figure 1. The multi-wavelength light curves display similar variability behavior as the γ -ray one. When the optical and MIR magnitudes were at their brightest during MJD 58500–58800, with the optical showing strong variation activity, the γ -ray flux (and TS value) was also at the

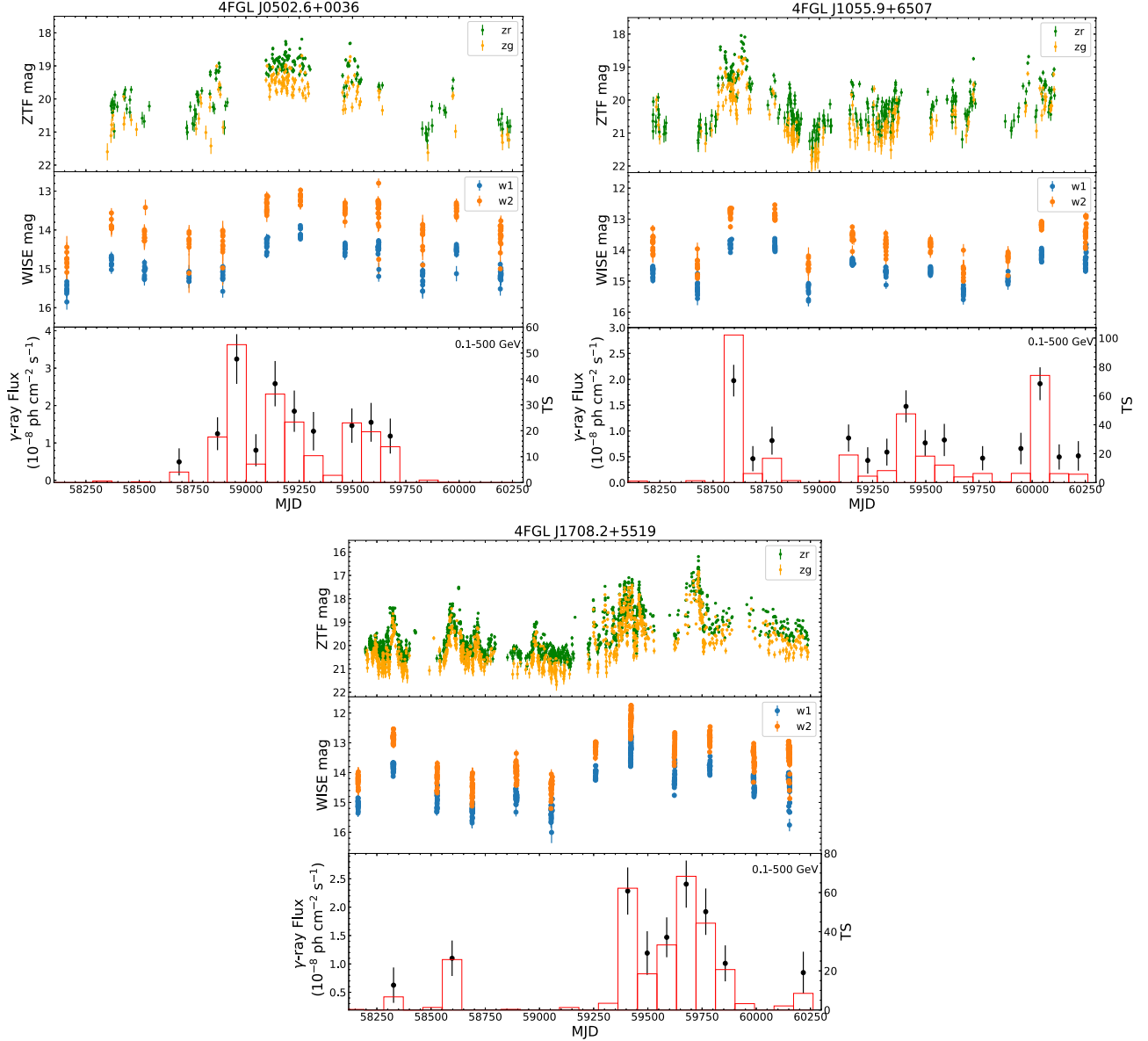


Figure 1. Multi-wavelength light curves for 4FGL J0502.6+0036, 4FGL J1055.9+6507, and 4FGL J1708.2+5519. The top and middle panels display the ZTF light curves in *zg* and *zr* bands and WISE MIR light curves in *w1* and *w2* bands, respectively. The bottom panels feature 90 day binned light curves in 0.1–500 GeV (black dots), while the corresponding TS values are indicated by red bars. The data points with $TS < 4$ are not kept in the light curves.

highest. Given both the spatial and temporal coincidence, NVSS J105533+650956 and PS2 are highly likely the radio and optical counterparts to 4FGL J1055.9+6507 respectively.

3.3. 4FGL J1708.2+5519

We performed the standard binned likelihood analysis on the data in 0.1–500 GeV for 4FGL J1708.2+5519, and the obtained best-fit $\Gamma = 2.41 \pm 0.11$, with a TS value of ≈ 171 , in agreement with those given in 4FGL-DR4. Using the same setting as that

for the above two sources, its 90 day binned light curve was extracted (see Figure A1). The light curve exhibits flare events, with a dominant one occurring approximately during MJD 59250–60000. The calculated $TS_{\text{var}} \approx 196.3$, indicating γ -ray flux variations of the source at an 8.1σ significance level.

From running `gtfindsrc`, we obtained R.A. = 257°05, decl. = +55°32 (equinox J2000.0), with a 2σ uncertainty of 0°04 (see Table 2). Within the error circle of the position, there is one radio source, NVSS J170802+551919, given in the SIMBAD database. The calculated TS map in 0.1–500 GeV

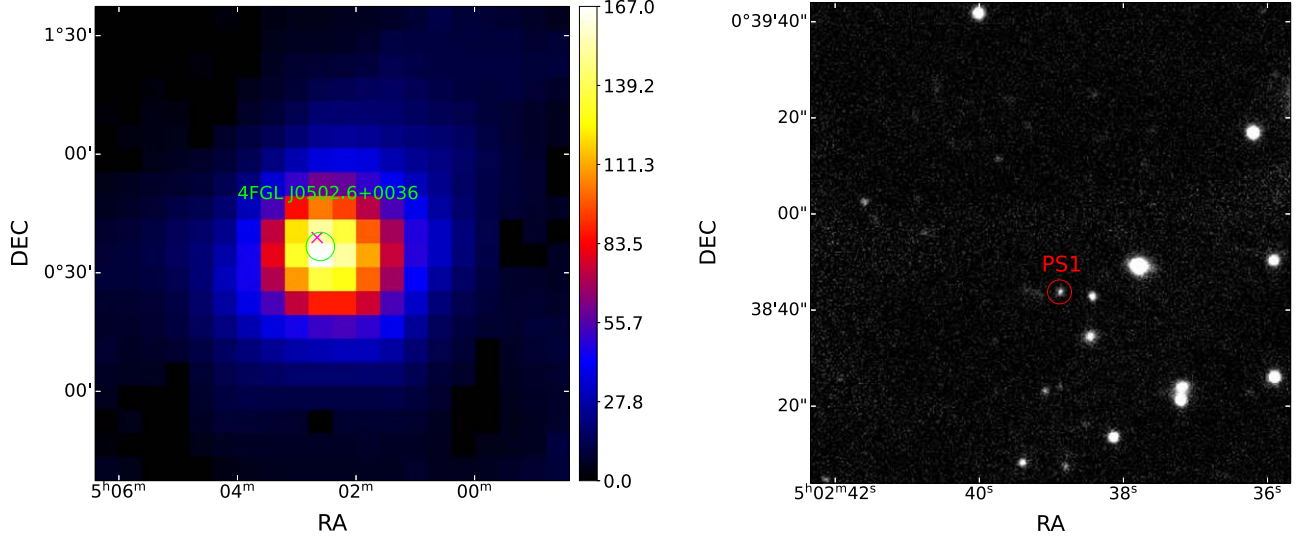


Figure 2. Left: 0.1–500 GeV $2^\circ \times 2^\circ$ TS map centered at 4FGL J0502.6+0036 during MJD 58600–59750, with its 2σ positional error circle marked as a green circle. The purple cross marks the location of the radio source BWE 0500+0034. Right: Pan-STARRS *i*-band $100'' \times 100''$ image centered at BWE 0500+0034. The optical source PS1 is indicated by a red circle.

Table 2
Comparison of Source Information in this Work and in 4FGL-DR4

Name	Reference	R.A. (deg)	Decl. (deg)	R_{95} (deg)	Γ_γ	TS
4FGL J0502.6+0036	4FGL-DR4	75.65	+0.61	0.05	2.24 ± 0.11	83
4FGL J0502.6+0036	This work	75.65	+0.61	0.06	2.13 ± 0.14	54
BWE 0500+0034	Becker et al. (1991)	75.66	+0.65
4FGL J1055.9+6507	4FGL-DR4	163.98	+65.13	0.05	2.32 ± 0.08	198
4FGL J1055.9+6507	This work	163.92	+65.14	0.04	2.25 ± 0.08	168
NVSS J105533+650956	Condon et al. (1998)	163.89	+65.17
4FGL J1708.2+5519	4FGL-DR4	257.05	+55.32	0.09	2.38 ± 0.09	167
4FGL J1708.2+5519	This work	257.05	+55.32	0.04	2.41 ± 0.11	171
FIRST J170802.8+551920	Helfand et al. (2015)	257.01	+55.32

Note. R_{95} is the error radius at a 95% confidence level; the value of 4FGL-DR4 is the average estimated from values of the semimajor axis and semiminor axis of the error ellipse at a 95% confidence level.

during the dominant-flare time period (MJD 59250–60000) shows the positional match between 4FGL J1708.2+5519 and the radio source (left panel of Figure 4). There is another radio source from the Faint Images of the Radio Sky at Twenty-cm (FIRST) survey, FIRST J170802.8+551920, which is slightly further away. The FIRST survey typically has a positional uncertainty of $0''.3$ (Helfand et al. 2015). We note that these two radio sources were matched as one in, for example, Flesch (2024). A 99.2% probability for the association between 4FGL J1708.2+5519 and FIRST J170802.8+551920 was estimated with `gtsrcid`, indicating their association is a highly likely case. The Pan-STARRS $10'' \times 10''$ image in *i*-band centered at

NVSS J170802+551919 is shown in the right panel of Figure 4. There is one optical source, named PS3 in this work, which positionally matches FIRST J170802.8+551920. Here again, the position of PS3 given in Pan-STARRS is $0''.3$ away from the peak of the optical source in the *i*-band image. The ZTF and WISE light curves of PS3 (Figure 1) feature concurrent variations with the γ -ray flaring events, especially the dominant one in MJD 59250–60000. Therefore given the closeness of the radio and optical sources and the similarity in temporal variations at multi-wavelengths, it is highly likely that the two radio sources are the same one and they and PS3 are the radio and optical counterparts of 4FGL J1708.2+5519 respectively.

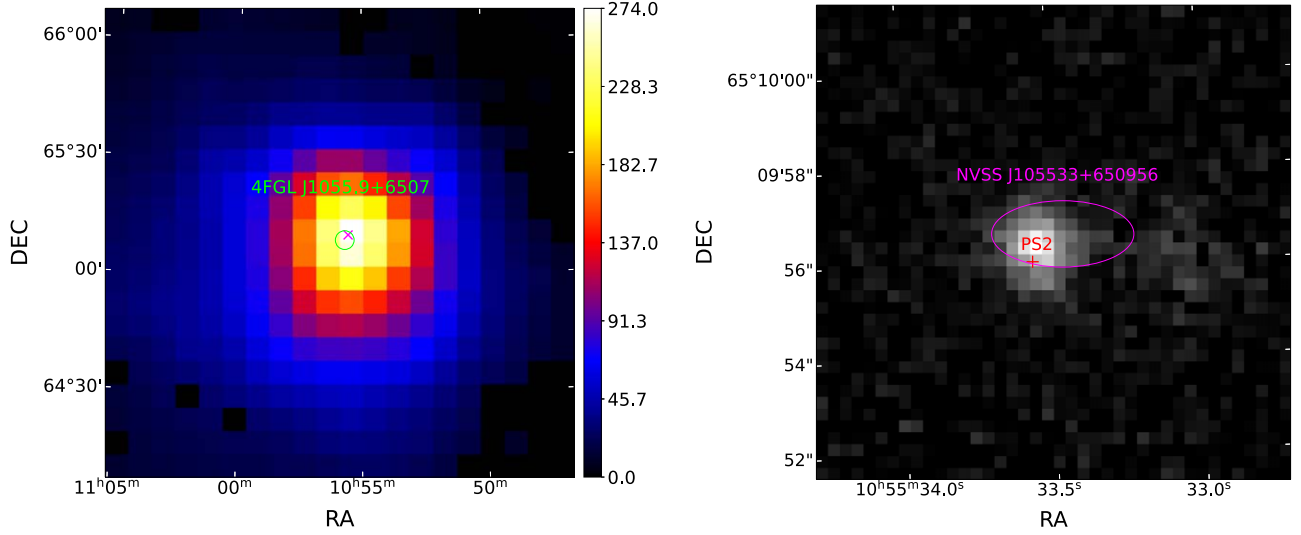


Figure 3. Left: 0.1–500 GeV $2^\circ \times 2^\circ$ TS map centered at 4FGL J1055.9+6507, with its 2σ positional error circle marked as a green circle. The purple cross is the location of the radio source NVSS J105533+650956. Right: Pan-STARRS i -band $10'' \times 10''$ image centered at NVSS J105533+650956. The positional error region of NVSS J105533+650956 is indicated by a purple ellipse, and the optical source PS2 is marked with a red cross. There is a $0''.3$ offset between the peak of the optical source and the position of PS2 given in Pan-STARRS.

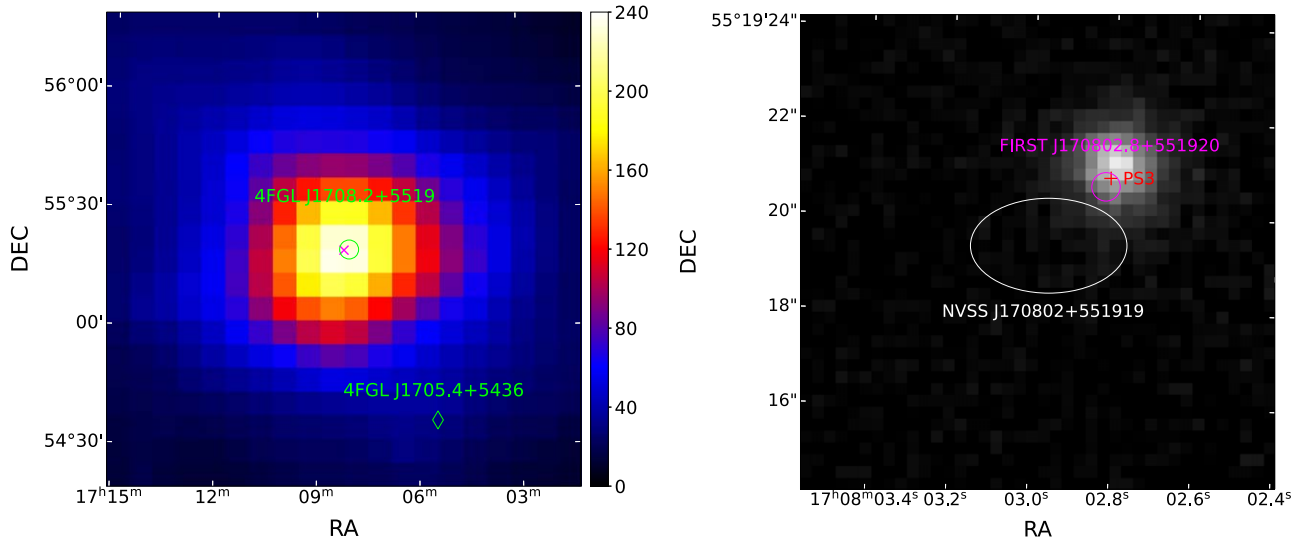


Figure 4. Left: 0.1–500 GeV $2^\circ \times 2^\circ$ TS map centered at 4FGL J1708.2+5519 during the flaring time period of MJD 59250–60000. The source's 2σ positional error circle is marked as a green circle, and the purple cross marks the location of the radio source FIRST J170802.8+551920. Right: Pan-STARRS i -band $10'' \times 10''$ image centered at NVSS J170802+551919, whose error region is marked by the white solid ellipse. The positional error circle of FIRST J170802.8+551920 is marked by a purple circle, which contains the optical source PS3 (the red cross). There is a $0''.3$ offset between the peak of the optical source and the position of PS3 given in Pan-STARRS.

3.4. Broadband Spectral Energy Distributions of the Three Sources

Given the identification established above, we built the broadband spectral energy distributions (SEDs) for the three sources. First we extracted the γ -ray spectrum for each of them. Using the best-fit models obtained above from the likelihood

analysis, we performed the maximum likelihood analysis on the data in 10 evenly divided energy bins in logarithm from 0.1 to 500 GeV. In this analysis, the spectral normalizations of the sources in a source model within 5° of each target source were set free, and all other spectral parameters of the sources were fixed at the best-fit values obtained in the likelihood analysis of

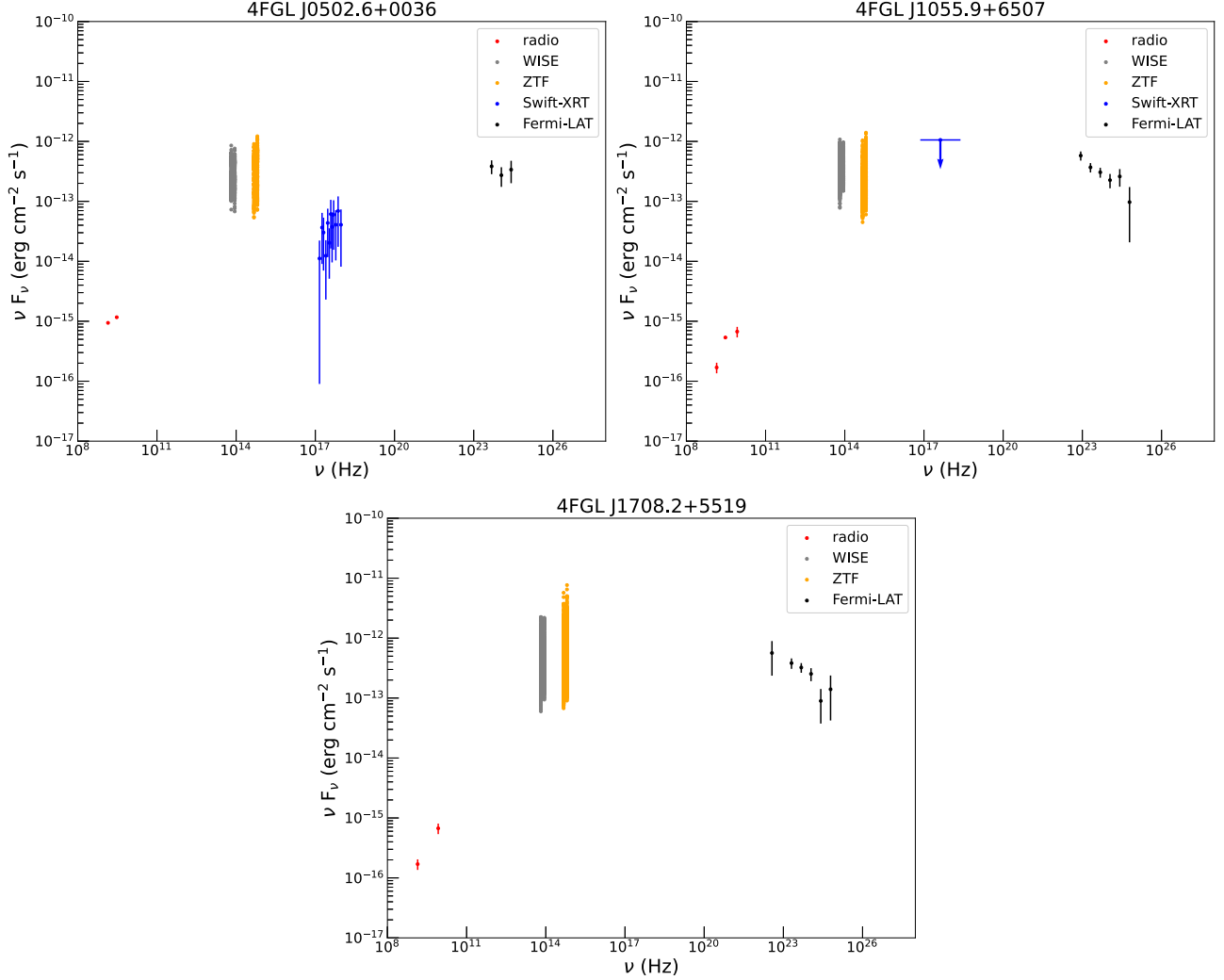


Figure 5. Broadband SEDs of 4FGL J0502.6+0036, 4FGL J1055.9+6507, and 4FGL J1708.2+5519. Archival radio flux measurements are red dots (from Condon et al. 1998; Helfand et al. 2015; Myers et al. 2003; Gordon et al. 2021), and MIR w1 and w2 and ZTF zr and zg fluxes (used in this work) are gray and yellow dots respectively. The Swift-XRT X-ray spectrum of 4FGL J0502.6+0036 is plotted as the blue dots (top-left panel), and the X-ray flux upper limit for 4FGL J1055.9+6507 is indicated by a blue arrow (top-right panel). The γ -ray spectra we obtained for the three sources are plotted as black dots in each panel.

the whole data. For the extracted γ -ray spectra, we only kept the data points with $TS \geq 4$.

The broadband SEDs of blazars often display two emission humps, a low-energy hump peaking at radio to ultraviolet/X-ray wavelengths and the other one at hard X-ray to γ -ray energies. In the leptonic model that is widely considered, the low-energy hump is produced from synchrotron radiation of relativistic electrons in jets while the high-energy one is generated by inverse Compton (IC) scattering of low-energy photons by the same population of the electrons (e.g., Sikora et al. 1994; Bloom & Marscher 1996). Given the X-ray detection of 4FGL J0502.6+0036, its SED appears to be in such a two-hump shape (Figure 5). We did not attempt to fit the SED with a typical leptonic model for blazars, since the data

were not simultaneous and had strong variations. For 4FGL J1055.9+6507 and 4FGL J1708.2+5519, their SEDs share similarity with that of 4FGL J0502.6+0036, although X-ray detection would help strengthen it. We checked the eROSITA X-ray data (Predehl et al. 2021), but unfortunately both 4FGL J1055.9+6507 and 4FGL J1708.2+5519 are not in the sky region of the recently released survey data.

4. Discussion

Among the AGNs detected by Fermi-LAT, blazars are the dominant ones (e.g., Ballet et al. 2023). In addition, there are also so-called Narrow Line Seyfert 1 (NLSy1) galaxies and RGs. The former are defined by their optical narrow Balmer

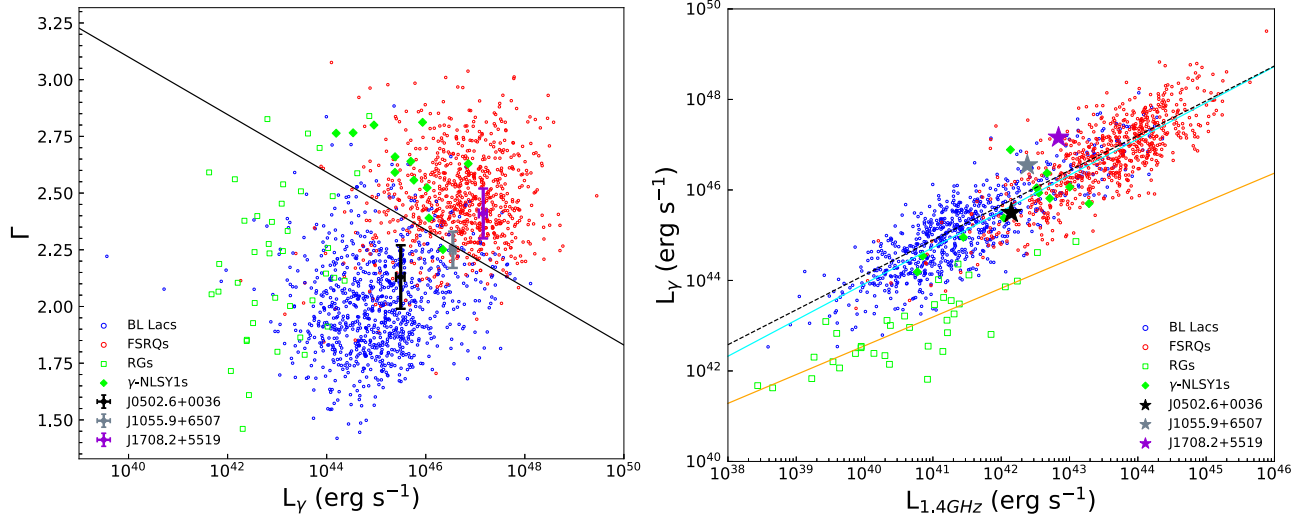


Figure 6. Left: γ -ray photon indices vs. γ -ray luminosities of different sub-types of AGNs, drawn from the information provided in 4LAC-DR3 (Ajello et al. 2022). The three sources in this work are marked. FSRQs and BL Lacs are possibly separated by a black line ($\Gamma = -0.127 \log L_\gamma + 8.18$; Chen 2018). Right: γ -ray luminosities vs. 1.4 GHz radio luminosities of γ -ray AGNs. The radio measurements at 1.4 GHz were obtained from the NED. The black dashed line is given by Wu et al. (2024) for blazars ($\log L_\gamma = 0.77 \log L_{1.4\text{GHz}} + 13.32$). The cyan and orange solid lines are the relationships for blazars and RGs, respectively, that we obtained in this work.

(the full-width at half maximum of $H_\beta < 2000 \text{ km s}^{-1}$), weak [O III], and strong Fe II emission lines (Osterbrock & Pogge 1985; Goodrich 1989). They are considered to be able to host relativistic jets similar to blazars (e.g., Abdo et al. 2009b; Paliya et al. 2014 and references therein) and thus exhibit multi-wavelength variability as well (e.g., Abdo et al. 2009b; Paliya et al. 2013, 2014; Paliya & Stalin 2016). At the γ -ray band, they show soft emission ($\Gamma > 2$), similar to FSRQs, but have γ -ray luminosities L_γ smaller than those of powerful FSRQs (Paliya et al. 2018; see also Figure 6). Studies of their broadband SEDs also show that they more closely resemble FSRQs than BL Lacs (e.g., Zhang et al. 2013; Sun et al. 2015). The latter, RGs, are considered as blazars with a misaligned jet. Most RGs have low redshifts; for example, the largest recorded distance for an RG has a redshift of 0.22 in the Fermi-LAT sample (Ajello et al. 2022). As a result, their γ -ray luminosities are generally lower than those of blazars (Figure 6). We note that Paliya et al. (2023) recently identified a distant γ -ray RG, TXS 1433+205, at $z = 0.748$, but it can be considered as an extreme case.

We checked the radio images for the three sources, and they all only show a core, without any structures seen. In the more recent radio data from the Australian Square Kilometre Array Pathfinder (ASKAP; Johnston et al. 2007, 2008; Hotan et al. 2021), 4FGL J0502.6+0036 is within the survey's field. There were six flux-density measurements at 887.5 MHz and one at 1367.5 MHz. The lowest and highest flux densities at 887.5 MHz were $52.7 \pm 0.4 \text{ mJy}$ and $74.4 \pm 0.5 \text{ mJy}$, respectively; the flux density at 1367.5 MHz was $57.4 \pm 0.4 \text{ mJy}$, while the NVSS's flux density was $67.2 \pm 0.9 \text{ mJy}$ at 1.4 GHz.

These measurements show that the source had significant flux variations at radio frequencies as well.

By the large fraction of blazars in the Fermi-LAT sample, the three sources in this work are likely blazars. Their multi-wavelength variabilities and SEDs all fit in this identification. In Flesch (2024), the redshifts of the optical counterparts to 4FGL J0502.6+0036, 4FGL J1055.9+6507, and 4FGL J1708.2+5519 are reported to be 0.6, 1.5, and 2.3, respectively, derived from photometric measurements. With the redshifts assumed, their locations in the L_γ - Γ plot (displayed in the left panel of Figure 6) can be found. As can be seen, they are more luminous than RGs, a fact seen in the comparison of the two sub-classes of AGNs in the Fourth LAT AGN Catalog (4LAC-DR3; Ajello et al. 2022): the mean redshift of blazars being ~ 0.8 while the mean redshift of RGs being ~ 0.05 . Also although with large uncertainties on their γ -ray photon indices, the three sources appear harder than most NLSy1 galaxies. FSRQs and BL Lacs can be relatively well separated in this plot (Abdo et al. 2009a; Ghisellini et al. 2009; Ackermann et al. 2015; Chen 2018), as FSRQs are more luminous with softer emission while BL Lacs are comparably the opposite. Chen (2018) obtained a criterion line ($\Gamma = -0.127 \log L_\gamma + 8.18$) to separate these two sub-types of blazars with a success rate of 88.6%. Following this criterion, we may classify 4FGL J0502.6+0036 as a BL Lac, 4FGL J1708.2+5519 as an FSRQ, and 4FGL J1055.9+6507 as either. Additionally, blazars and RGs may also be separated in a L_γ - $L_{1.4\text{GHz}}$ plot. We obtained the 1.4 GHz radio data from the NASA/IPAC Extragalactic Database⁵ (NED), and performed a

⁵ <https://ned.ipac.caltech.edu/>

linear fitting between $\log L_\gamma$ and $\log L_{1.4\text{GHz}}$ for blazars and RGs, respectively. For blazars, we obtained a relationship of $\log L_\gamma = (0.80 \pm 0.01)\log L_{1.4\text{GHz}} + (11.9 \pm 0.4)$, which is close to the fitting result reported by Wu et al. (2024). For RGs, the relationship we obtained was $\log L_\gamma = (0.64 \pm 0.08)\log L_{1.4\text{GHz}} + (17.1 \pm 3.2)$. These two relationships are depicted in the right panel of Figure 6. As can be seen, the three sources are among blazars and lie close to the relationship of blazars.

Follow up optical spectroscopy and X-ray observations of the three sources are warranted. The first studies can obtain the spectral features that would further identify them as a BL Lac or FSRQ, or an extreme RG or NLSy1 galaxy and possibly determine their redshifts. The latter will help obtain their X-ray emission properties that help better their SEDs. In addition, this work exemplarily demonstrates a procedure for identification of Fermi-LAT unidentified sources, given the advent of rich data from large, multi-wavelength surveys. A potential radio counterpart will help lower the several-arcminute positional uncertainties of Fermi-LAT sources to a region of a few arcseconds, and multi-wavelength variability analysis will identify the likely counterpart.

Acknowledgments

This work was based on observations obtained with the Samuel Oschin Telescope 48 inch and the 60 inch Telescope at the Palomar Observatory as part of the Zwicky Transient Facility project. ZTF is supported by the National Science Foundation under grant No. AST-2034437 and a collaboration including Caltech, IPAC, the Weizmann Institute for Science, the Oskar Klein Center at Stockholm University, the University of Maryland, Deutsches Elektronen-Synchrotron and Humboldt University, the TANGO Consortium of Taiwan, China, the University of Wisconsin at Milwaukee, Trinity College Dublin, Lawrence Livermore National Laboratories, and IN2P3, France. Operations are conducted by COO, IPAC,

and UW. This publication makes use of data products from the Near-Earth Object Wide-field Infrared Survey Explorer (NEOWISE), which is a joint project of the Jet Propulsion Laboratory/California Institute of Technology and the University of Arizona. NEOWISE is funded by the National Aeronautics and Space Administration. This research has made use of the SIMBAD database, operated at CDS, Strasbourg, France. This research has made use of the NASA/IPAC Extragalactic Database, which is funded by the National Aeronautics and Space Administration and operated by the California Institute of Technology. This work uses data obtained from Inyarrimanha Ilgari Bundara/the Murchison Radio-astronomy Observatory. We acknowledge the Wajarri Yamaji People as the Traditional Owners and native title holders of the Observatory site. CSIROs ASKAP radio telescope is part of the Australia Telescope National Facility (<https://ror.org/05qajvd42>). Operation of ASKAP is funded by the Australian Government with support from the National Collaborative Research Infrastructure Strategy. ASKAP uses the resources of the Pawsey Supercomputing Research Centre. Establishment of ASKAP, Inyarrimanha Ilgari Bundara, the CSIRO Murchison Radio-astronomy Observatory and the Pawsey Supercomputing Research Centre are initiatives of the Australian Government, with support from the Government of Western Australia and the Science and Industry Endowment Fund. This paper includes archived data obtained through the CSIRO ASKAP Science Data Archive, CASDA (<http://data.csiro.au>).

We thank the referee for helpful suggestions. This research is supported by the Basic Research Program of Yunnan Province (No. 202201AS070005), the National Natural Science Foundation of China (NSFC, grant No. 12273033), and the Original Innovation Program of the Chinese Academy of Sciences (E085021002). S.J. acknowledges the support of the science research program for graduate students of Yunnan University (KC-23234629).

Appendix Long-term γ -Ray Light Curves

In Figure A1, the long-term γ -ray light curves of 4FGL J0502.6+0036, 4FGL J1055.9+6507, and 4FGL J1708.2+5519 are shown.

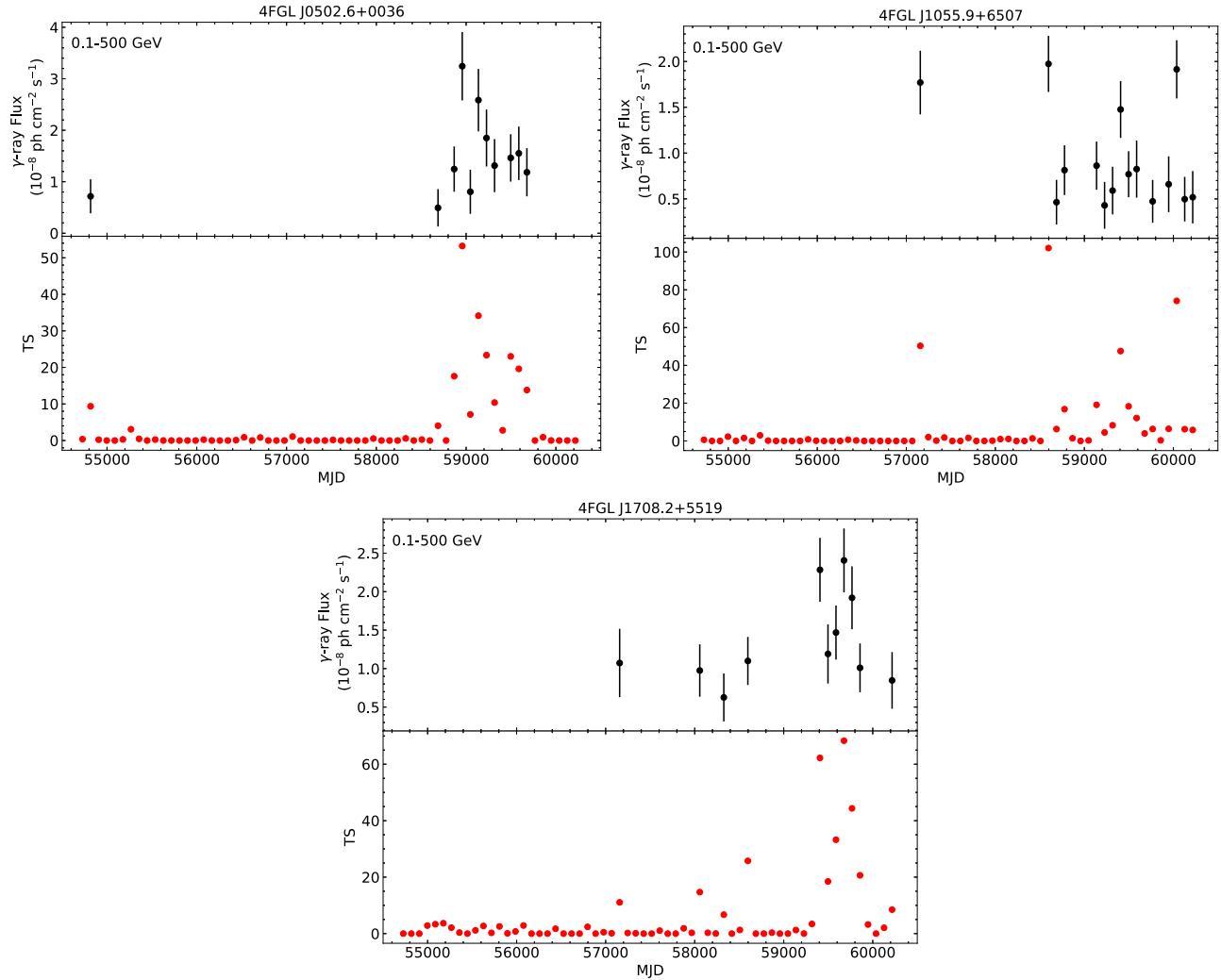


Figure A1. 90 day binned light curves (top) and TS curves (bottom) in 0.1–500 GeV for 4FGL J0502.6+0036, 4FGL J1055.9+6507, and 4FGL J1708.2+5519. Fluxes with $TS \geq 4$ are kept in the light curves.

References

- Abdo, A. A., Ackermann, M., Ajello, M., et al. 2009a, *ApJ*, **700**, 597
 Abdo, A. A., Ackermann, M., Ajello, M., et al. 2009b, *ApJ*, **707**, 727
 Abdo, A. A., Ackermann, M., Ajello, M., et al. 2010, *ApJ*, **722**, 520
 Ackermann, M., Ajello, M., Atwood, W. B., et al. 2015, *ApJ*, **810**, 14
 Ackermann, M., Ajello, M., Albert, A., et al. 2016, *PhRvL*, **116**, 151105
 Ajello, M., Baldini, L., Ballet, J., et al. 2022, *ApJS*, **263**, 24
 Ajello, M., Gasparrini, D., Sánchez-Conde, M., et al. 2015, *ApJL*, **800**, L27
 Atwood, W. B., Abdo, A. A., Ackermann, M., et al. 2009, *ApJ*, **697**, 1071
 Ballet, J., Bruel, P., Burnett, T. H., Lott, B. & The Fermi-LAT collaboration 2023, arXiv:2307.12546
 Becker, R. H., White, R. L., & Edwards, A. L. 1991, *ApJS*, **75**, 1
 Bellm, E. C., Kulkarni, S. R., Graham, M. J., et al. 2019, *PASP*, **131**, 018002
 Blandford, R. D., & Payne, D. G. 1982, *MNRAS*, **199**, 883
 Blandford, R. D., & Znajek, R. L. 1977, *MNRAS*, **179**, 433
 Bloom, S. D., & Marscher, A. P. 1996, *ApJ*, **461**, 657
 Chambers, K. C., Magnier, E. A., Metcalfe, N., et al. 2016, arXiv:1612.05560
 Chen, L. 2018, *ApJS*, **235**, 39
 Chiaro, G., Kovacevic, M., & La Mura, G. 2021, *JHEAp*, **29**, 40
 Condon, J. J., Cotton, W. D., Greisen, E. W., et al. 1998, *AJ*, **115**, 1693
 Di Mauro, M., Calore, F., Donato, F., Ajello, M., & Latronico, L. 2014, *ApJ*, **780**, 161
 Di Mauro, M., Manconi, S., Zechlin, H. S., et al. 2018, *ApJ*, **856**, 106

- Evans, P. A., Beardmore, A. P., Page, K. L., et al. 2007, *A&A*, **469**, 379
- Evans, P. A., Beardmore, A. P., Page, K. L., et al. 2009, *MNRAS*, **397**, 1177
- Evans, P. A., Page, K. L., Osborne, J. P., et al. 2020, *ApJS*, **247**, 54
- Fan, J. H., Yang, J. H., Xiao, H. B., et al. 2017, *ApJL*, **835**, L38
- Flesch, E. W. 2024, *OJAp*, **7**, 6
- Fukazawa, Y., Matake, H., Kayanoki, T., Inoue, Y., & Finke, J. 2022, *ApJ*, **931**, 138
- Ghisellini, G., Maraschi, L., & Tavecchio, F. 2009, *MNRAS*, **396**, L105
- Ghisellini, G., Righi, C., Costamante, L., & Tavecchio, F. 2017, *MNRAS*, **469**, 255
- Ghisellini, G., & Tavecchio, F. 2008, *MNRAS*, **387**, 1669
- Ghisellini, G., Tavecchio, F., Foschini, L., Bonnoli, G., & Tagliaferri, G. 2013, *MNRAS*, **432**, L66
- Goodrich, R. W. 1989, *ApJ*, **342**, 224
- Gordon, Y. A., Boyce, M. M., O’Dea, C. P., et al. 2021, *ApJS*, **255**, 30
- Hayashida, M., Nalewajko, K., Madejski, G. M., et al. 2015, *ApJ*, **807**, 79
- Helfand, D. J., White, R. L., & Becker, R. H. 2015, *ApJ*, **801**, 26
- HI4PI Collaboration, Ben Bekhti, N., Flöer, L., et al. 2016, *A&A*, **594**, A116
- Hotan, A. W., Bunton, J. D., Chippendale, A. P., et al. 2021, *PASA*, **38**, e009
- Johnston, S., Bailes, M., Bartel, N., et al. 2007, *PASA*, **24**, 174
- Johnston, S., Taylor, R., Bailes, M., et al. 2008, *ExA*, **22**, 151
- Kaur, A., Kerby, S., & Falcone, A. D. 2023, *ApJ*, **943**, 167
- Mainzer, A., Bauer, J., Cutri, R. M., et al. 2014, *ApJ*, **792**, 30
- Medford, M. S., Lu, J. R., & Schlafly, E. F. 2020, *RNAAS*, **4**, 38
- Myers, S. T., Jackson, N. J., Browne, I. W. A., et al. 2003, *MNRAS*, **341**, 1
- Nolan, P. L., Abdo, A. A., Ackermann, M., et al. 2012, *ApJS*, **199**, 31
- Osterbrock, D. E., & Pogge, R. W. 1985, *ApJ*, **297**, 166
- Paliya, V. S., Ajello, M., Rakshit, S., et al. 2018, *ApJL*, **853**, L2
- Paliya, V. S., Sahayanathan, S., Parker, M. L., et al. 2014, *ApJ*, **789**, 143
- Paliya, V. S., Saikia, D. J., & Stalin, C. S. 2023, *MNRAS*, **520**, L33
- Paliya, V. S., & Stalin, C. S. 2016, *ApJ*, **820**, 52
- Paliya, V. S., Stalin, C. S., Kumar, B., et al. 2013, *MNRAS*, **428**, 2450
- Patel, S. R., Chitnis, V. R., Shukla, A., Rao, A. R., & Nagare, B. J. 2018, *ApJ*, **866**, 102
- Predehl, P., Andritschke, R., Arefiev, V., et al. 2021, *A&A*, **647**, A1
- Scarpa, R., & Falomo, R. 1997, *A&A*, **325**, 109
- Shukla, A., Mannheim, K., Patel, S. R., et al. 2018, *ApJL*, **854**, L26
- Sikora, M., Begelman, M. C., & Rees, M. J. 1994, *ApJ*, **421**, 153
- Sun, X.-N., Zhang, J., Lin, D.-B., et al. 2015, *ApJ*, **798**, 43
- Urry, C. M., & Padovani, P. 1995, *PASP*, **107**, 803
- Wright, E. L., Eisenhardt, P. R. M., Mainzer, A. K., et al. 2010, *AJ*, **140**, 1868
- Wu, T.-Z., Yu, Y.-W., Gan, Y.-Y., Zhang, H.-M., & Zhang, J. 2024, *ApJ*, **967**, 137
- Yi, T.-F., Zhang, J., Lu, R.-J., Huang, R., & Liang, E.-W. 2017, *ApJ*, **838**, 34
- Zhang, J., Sun, X. N., Zhang, S. N., & Liang, E. W. 2013, in *Feeding Compact Objects: Accretion on All Scales*, Vol. 290, ed. C. M. Zhang et al. (Cambridge: Cambridge Univ. Press), 359
- Zhu, K. R., Chen, J. M., Zheng, Y. G., & Zhang, L. 2024, *MNRAS*, **527**, 1794